Volume 6 | Number 32 | 28 August 2018 | Pages 8559–8848

Journal of Materials Chemistry C

Materials for optical, magnetic and electronic devices

rsc.li/materials-c

ISSN 2050-7526

PAPER

Dongpo Song, Xuebin Zhu *et al.*

Evolution of structure and ferroelectricity in Aurivillius $Bi_4Bi_{n-3}Fe_{n-3}Ti_3O_{3n+3}$ thin films

Journal of Materials Chemistry C

PAPER

Cite this: J. Mater. Chem. C, 2018, 6, 8618

Evolution of structure and ferroelectricity in Aurivillius $Bi_4Bi_{n-3}Fe_{n-3}Ti_3O_{3n+3}$ thin films†

Dongpo Song, *[a] Jie Yang,[a] Bingbing Yang,[b] Liangyu Chen,[a] Fang Wang[a] and Xuebin Zhu *[b]

Received 10th May 2018, Accepted 6th June 2018

DOI: 10.1039/c8tc02270d

rsc.li/materials-c

Ferroelectric Aurivillius thin films $Bi_4Bi_{n-3}Fe_{n-3}Ti_3O_{3n+3}$ (BFTO n = 3, 4, 5, 6) were successfully prepared on platinum-coated silicon substrate by chemical solution deposition and the ferroelectric polarization properties were investigated and detailed. Simultaneously, the dielectric and leakage current characteristics of the thin films were obtained. Evolution of the Aurivillius layer structure was confirmed by XRD and HR-TEM results. A saturated hysteresis loop with larger remanent polarization ($2P_r$) and excellent retention properties are observed in all thin films. The values of $2P_r$ in the film capacitors are all about 50 μC cm^{-2} besides the n = 3 film, in which the leakage current increases significantly in larger electric fields. The leakage current values of films $Bi_5FeTi_3O_{15}$, $Bi_6Fe_2Ti_3O_{18}$ and $Bi_7Fe_3Ti_3O_{21}$ gradually increased with increasing n, and the leakage current mechanism was studied by various conduction mechanisms. The combined relationships of the ferroelectric polarization, leakage current, polarization fatigue and retention of BFTO thin films are discussed in terms of the structural characteristics, aggregation of oxygen vacancies and crystallite grain size in the films. The results of optimization of the ferroelectric properties in Aurivillius phase thin films with higher n by chemical solution deposition are useful for further exploration of single-phase multiferroics in the Aurivillius family and other layer structure compounds with potential applications in the field of ferroelectric-based data storage.

Introduction

Aurivillius phases (also called Bi-based layer structure materials) with the generic formula $(Bi_2O_2)^{2+}(A_{n-1}B_nO_{3n+1})^{2-}$ (A = Na, K, Ca, Sr, Ba, Pb, Bi, *etc.*, and B = Ti, Fe, *etc.*) have a naturally layered perovskite-related crystal structure that consists of perovskite-like $(A_{n-1}B_nO_{3n+1})^{2-}$ layers interleaved between fluorite-like $(Bi_2O_2)^{2+}$ layers, where n refers to the number of perovskite-like layers (see middle of Fig. 1). The first ferroelectric compound with Aurivillius phase structure was $PbBi_2Nb_2O_9$, discovered by Smolenski and Agranovskaya in 1959.[1] Then, Smolenski *et al.* and Subbarao confirmed ferroelectric properties for a large number of Bi-based layer structure materials with the above general formula.[2] Combined with fatigue-free behavior, good retention characteristic and lower leakage currents, lower n $SrBi_2Ta_2O_9$-based (SBT n = 2) Aurivillius compounds were commercialized as ferroelectric random access memory (FeRAM) by Ramtron in the 1990s. By contrast, $Bi_4Ti_3O_{12}$-based (n = 3) ferroelectrics, which are considered to be adding one perovskite-like layer, revealed a serious fatigue problem. This issue received in-depth and extensive research and soon the substitution of rare-earth ions for Bi at the A-site showed nearly fatigue-free behavior. The entirely different fatigue behaviors have been attributed to the different nature of oxygen vacancy defects between n = 2 and 3. From this perspective, perhaps, the higher n Aurivillius ferroelectrics received more attention until recent years as new physical natures were found and preparation technology advanced.[3]

Bismuth layered Aurivillius compounds, $Bi_4Bi_{n-3}Fe_{n-3}Ti_3O_{3n+3}$ (BFTO $n \geq 3$), have been attracting much attention in recent years not only due to the admirable abundance with fundamental physics (mainly focused on the coexistence of ferromagnetism and ferroelectricity and high ferroelectric (FE) phase transition temperatures) but also the great application potential as multi-level memory storage media, emergent spintronic technologies, energy harvesting, sensors and actuators.[4–10] The BFTO compounds are naturally layered of perovskite-related crystal structure, which consists of perovskite-like $(Bi_{n-1}Fe/Ti_nO_{3n+1})^{2-}$ octahedral layers interleaved between two fluorite-like $(Bi_2O_2)^{2+}$ layers, where the n refers to the number of perovskite-like layers. The perovskite-like Fe/Ti–O octahedral layers are responsible for the ferroelectricity and the (anti-)ferromagnetism.[11] The origin of ferroelectricity in the Aurivillius family is a combination of octahedral rotations and polar distortions, and the origin of the magnetism has been proposed based on the spin canting of magnetic sublattices *via*

[a] Department of Physics, Jiangsu University of Science and Technology, Zhenjiang, 212003, P. R. China. E-mail: dpsong@just.edu.cn
[b] Key Laboratory of Materials Physics, Institute of Solid State Physics, Chinese Academy of Sciences, Hefei 230031, P. R. China. E-mail: xbzhu@issp.ac.cn

† Electronic supplementary information (ESI) available. See DOI: 10.1039/c8tc02270d

This journal is © The Royal Society of Chemistry 2018

the Dzyaloshinskii–Moriya interaction.[12,13] The fluorite-like $(Bi_2O_2)^{2+}$ layers usually take charge of the reinforced resistance in Aurivillius compounds. The absence of fatigue in SBT is attributed to these bismuth oxide double layers by interaction with space charge compensation near the electrodes.

It is reasonable that the layer number (hereafter means perovskite-layers in Aurivillius compounds) of BFTO compounds could deeply influence their physical properties. The room temperature ferromagnetism (FM) in these BFTO compounds is very weak, which is far from the practical application requirements, and is generally due to their paraferromagnetic (PFM) or antiferromagnetic (AFM) nature. Improved ferromagnetism at room temperature has already been obtained by Co-doping in ceramic or thin films, and the effect of layer number on ferromagnetic properties has also been reported recently.[13–18] However, the observations of the ferroelectric polarization properties of different layer numbers showed a larger difference from past literature, in spite of the ferroelectric transition temperature being independent of the layer number, n.[19] The ferroelectric hysteresis loops of most ceramics and thin films present an obviously typical 'banana' loop shape.[20] We speculate that this hysteresis loop is unsatisfactory, both from the perspective of scientific research and from the perspective of material applications. Our recent results revealed that authentic larger remanent polarization can be obtained in $n = 5$ Aurivillius compounds by facile chemical solution deposition.[21] However, it is a pity that real hysteresis loops of $n > 3$ and a systematic investigation of the influence of layer number n on the ferroelectric properties of BFTO have not been reported before. Meanwhile, owing to the almost equal Gibbs free energies of different-layered BFTO compounds and the inner constraint of crystalline structures, which increases with increasing n, it is really difficult to synthesize pure phase BFTO compounds with $n > 6$.[14] In this work, pristine $Bi_4Bi_{n-3}Fe_{n-3}Ti_3O_{3n+3}$ (BFTO, n = 3–6) thin films were synthesized successfully, with a goal of contributing to the in-depth understanding of the ferroelectric properties and layer number n effects through intensive experiments.

Experimental

BFTO thin films with n = 3, 4, 5 and 6 were prepared by chemical solution deposition. Details of the solution preparation and spin coating processing can be found in our previous work.[22] The precursor sol for the BFTO3 films, for example, was prepared by first dissolving appropriate amounts of bismuth acetate $[Bi(CH_3COO)_3]$ in an acidic solution using a magnetic stirrer. 5 mol% excess bismuth acetate was used to compensate the Bi loss that was induced during the thermal annealing of amorphous films. A stoichiometric amount of tetrabutyl titanate $[Ti(OC_4H_9)_4]$ solution was slowly added to the mixed precursor solution. Then the solution was further stirred at room temperature for more than 6 h. Coating solutions for the preparation of n = 4, 5, and 6 thin films were prepared using a similar approach as mentioned above with corresponding stoichiometric iron(II) acetate $[Fe(CH_3COO)_2]$ as the precursor. The resulting sols are stable for months.

Thin films were deposited onto commercial 10 mm × 10 mm polycrystalline platinum-coated silicon substrates. The used substrates were successively cleaned by acetone and ethanol in ultrasonic baths, and the final cleaning was carried out in a plasma cleaner. The coating procedure was performed at ambient atmosphere with a rotation speed of 6000 rpm and a time of 20 s. After drying each coating on a hot plate, the spin-coated thin films were baked at 400 °C in preheated tube furnaces for 10 min in air atmosphere. The processes of spin-coating and pyrolysis were repeated ten times to increase the thin film thickness. Then, the baked films were annealed in a 750 °C preheated tube furnace in air atmosphere for 30 min. For the sake of simplicity, the thin films with different perovskite-like n = 3, 4, 5 and 6 are defined as BFTO3, BFTO4, BFTO5, BFTO6, respectively. The finally thickness of the films with n = 3, 4, 5 and 6 is approximately 315, 315, 338 and 463 nm, respectively, according to the corresponding cross-section profile obtained by scanning electron microscopy.

The crystalline structures of the as-fabricated samples were determined using a Philips X'Pert PRO X-ray diffractometer (XRD) with Cu-K_α radiation at room temperature. The surface microstructures and thicknesses of the films were determined by field emission scanning electron microscopy (FE-SEM, Sirion 200, FEI Company, USA). High-resolution transmission electron microscopy (HR-TEM) images and selected area electron diffraction (SAED) patterns were obtained with a JEM-2010 transmission electron microscope (JEM-2010, JEOL Ltd, Japan). Dielectric measurements were performed in the frequency range of 100 Hz–1 MHz using a driving voltage of 0.5 V with a precision LCR meter (TH2828/A/S). The ferroelectric and leakage properties were measured using a Sawyer-Tower circuit attached to a computer-controlled standardized ferroelectric test system (Precision Premier II, Radiant Technology, USA). Top Au electrodes with a diameter of 0.2 mm were sputtered to measure the electrical properties.

Results and discussion

Crystallography and microstructure

Most Aurivillius phases have many features in common at the structural and functional levels. The tetragonal $I4/mmm$ space group (beyond Bi_2WO_6) can be seen as the prototypical high-symmetry reference structure for the whole family at high temperatures, while at low temperatures the majority of Aurivillius phases take a polar orthorhombic (or monoclinic) ground-state with similar a and b cell parameters. Typically, this ground-state is ferroelectric and exhibits a large spontaneous polarization ($\approx$30–50 μC cm^{-2}) and high Curie temperature ($T_c > 600$ K).[12] The room temperature XRD patterns of the BFTO thin films (see Fig. S1, ESI†) indicate that the samples are of single phase with no detectable secondary phases. The patterns of the samples can be indexed with corresponding space groups owing to their different crystal structure and symmetry. The patterns of BFTO3 and BFTO5 films can be indexed with an orthorhombic lattice with the space groups $Fmmm$ and $B2cb$, respectively. The patterns of BFTO4 and BFTO6 films can be indexed with an orthorhombic

lattice with the space groups *Fmm*2 and *A*21*am*, respectively. This is in agreement with previous results.[15,23] All samples are of random orientation and no other impurity diffraction peaks can be detected, such as $BiFeO_3$, indicating the formation of a single phase of Aurivillius structure.

The peak located at $2\theta \approx 30^{\circ}$ shifted towards the larger angle slightly as the layer number n increased, which further indicated a successful synthesis of the desired layer-structured BFTO samples. The lattice parameter c was determined to be 3.237(4) nm, 4.128(7) nm, 4.948(8) nm, and 5.714(1) nm for the samples with n = 3, 4, 5, and 6, respectively. It is noteworthy that BFTO3 thin films exhibit more *c*-axis orientation than others in the small angle region. This preferential orientation characteristic was widely reported in previous literature.[24] For the obtained XRD results, the Lotgering factor (f) was calculated to estimate the degree of *c*-orientation using the following formula: $f = p - p_0/1 - p_0$, where $p_0 = \sum \mathrm{I}(00l)/\sum \mathrm{I}(hkl)$ indicates the proportion of (00*l*) intensities to the total (*hkl*) intensities for a randomly oriented material (based on their corresponding standard PDF card), and p indicates the intensity proportion for a specified sample.[25] f = 1 and f = 0 indicate full texture and random texture, respectively. The orientation preference with the *c*-axis is obviously suppressed when increasing the n values from 3 to 4, as the Lotgering factors for the BFTO3 and BFTO4 samples are f = 0.89 and f = 0.24, respectively, while the Lotgering factors for the BFTO4, BFTO5 and BFTO6 samples show almost no significant changes, approximately 0.26, as shown in Fig. 4(d). As the n increases, the preferential orientation feature will fade away unless using a single crystal substrate or doping selection element. The essentially physical reason for this phenomenon is not clear yet. The inner constraint of the crystalline structures could be used as one of the factors owing to the larger crystallography aspect ratio of the Aurivillius phase increasing linearly with n. The cut-off surface energy may play a role in the orientation selectivity features, which has been reported in other ferroelectrics, such as $BaTiO_3$.[26]

Further insights into the layer structures of the prepared films are obtained by using HR-TEM due to the similar XRD results for Aurivillius structures with near $(A_{n-1}B_nO_{3n+1})^{2-}$ layers. Fig. 1 shows the HR-TEM results for the derived thin films and the SAED patterns are also given in the corresponding position. All samples show a homogeneous crystal structure with several perovskite layers sandwiched by two $(Bi_2O_2)^{2+}$ layers, which is analogous to the results for other reported Aurivillius compounds.[14–16,27] For instance, the sample with n = 4, as shown in Fig. 1(B-a), has a clearly formed stacked

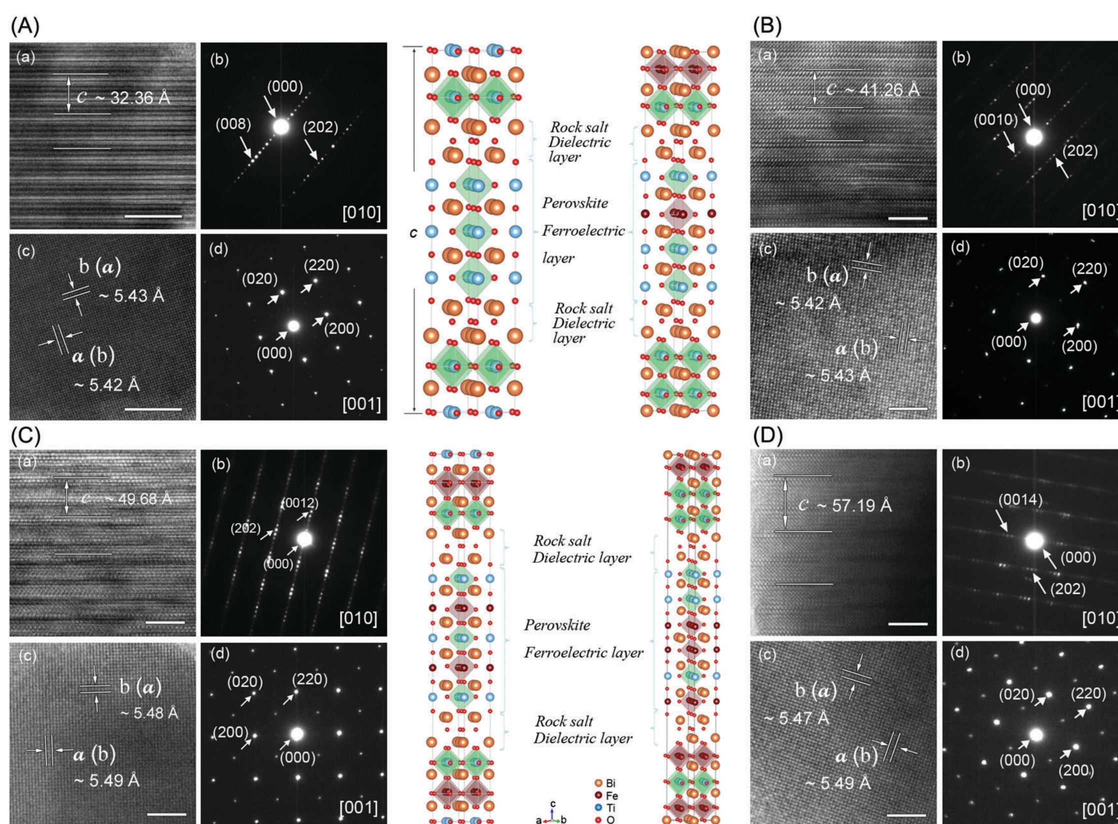

Fig. 1 The microstructures and single cell crystal structures of (A) BFTO3, (B) BFTO4, (C) BFTO5, (D) BFTO6. The rock salt dielectric layers and perovskite ferroelectric layers are arranged alternatively along the crystallographic direction of the c-axis. It is worth noting that the central perovskite layer of BFTO4 shown in brown (Fe–O octahedra) on the left side of (B) is a schematic description of the BFTO4. In reality, Fe or Ti occupied octahedra may distribute randomly in a disordered fashion within the four sandwiched perovskite layers. This feature is also agreed in the higher n compounds, as shown in the crystal structure schematic in the middle of Fig. 1. Presently, accurate experimental determination of the distribution of Ti and Fe cations is difficult. For example, the Rietveld refinement is less sensitive to the ordering of both cations owing to the similar X-ray scattering powers. The scale bar is 5 nm.

 This journal is © The Royal Society of Chemistry 2018

structure with four perovskite-like layers sandwiched between two fluorite-like $(Bi_2O_2)^{2+}$ layers, the three solid lines are guides for the periodicity, and relevant *c*-axis lattice constants are comparable to the values calculated from the XRD results. The in-plane lattice structure of the derived film is given in Fig. 1 (B-c) and the corresponding cubic-like SAED pattern (Fig. 1(B-d)) suggests that the obtained film's in-plane lattice constants are 5.42(4) Å and 5.43(6) Å. These values are slightly smaller than the values of a = 5.4611(2) Å and b = 5.4538(2) Å calculated from XRD measurement.

For the n = 3, 5 and 6 samples, similar results with a layered structure and SAED patterns are shown in Fig. 1(A), (C) and (D), respectively. It can be seen that the in-plane lattice constants of these four Aurivillius compounds are very close, while the out-of-plane lattice constant gradually increased. Although the natural layered structure is not an exclusive characteristic of the Aurivillius phase, it has special significance to ferroelectric research owing to the pure artificial ferroelectric superlattice having exceptional polarization performance but being difficult to grow. To give a clear contrast image of the layered structure, a structural view of the orthorhombic unit cell along the *c*-axis for the Aurivillius compounds with n = 4 is shown in the left side of Fig. 1(B). The rock salt dielectric layers and perovskite ferroelectric layers are arranged alternatively along the crystallographic direction of the *c*-axis. It is worth noting that the central perovskite layer of BFTO4 shown in brown (Fe–O octahedra) on the left side of Fig. 1(B) is a schematic description of the $BFTO_4$. A slight preference for the "inner" site was reported recently, while Fe or Ti occupied octahedra may distribute randomly in a disordered fashion within the four sandwiched perovskite layers.[28,29] This feature is also observed in the higher n compounds as the crystal structure schematic shows in the middle of Fig. 1. Presently, accurate experimental determination of the Ti^{4+} and Fe^{3+} cation distribution is difficult to obtain.[30] For example, the Rietveld refinement is less sensitive to the ordering of both cations owing to the similar X-ray scattering powers.

Leakage properties

The leakage current density (J) at room temperature was measured for all derived samples and the results on a semi-log scale on the electric field (E) with different n are shown in Fig. 2(a). Two features are noticeable. First, the leakage values of BFTO3 display a sharp rise in the field of approximately 150 kV cm^{-1}, and two orders of magnitude higher than J of other films under the field of approximately 200 kV cm^{-1}. Second, the leakage values of the BFTOs gradually increased with the increasing of n from 4 to 6. At an applied electric field of 200 kV cm^{-1} the leakage current density of the BFTO4 thin film was 1.34×10^4 A cm^{-2} and the corresponding measurements for the BFTO5 and BFTO6 thin films were 3.52×10^4 and 7.89×10^4 A cm^{-2}, respectively. To clarify the effects of the perovskite-like layer number n on J, the dependence of J measured at the positive maximum electric field (J_{max}) on the n is shown in Fig. 4. The J_{max} values of the films BFTO4, BFTO5 and BFTO6 gradually increased with the increasing of n. It is believed that the leakage current is lower in the smaller grain size films. The increased J of the BFTOs film is observed. However, the grain size of the BFTO4, BFTO5 and BFTO6 thin films according to the SEM results (see Fig. S2, ESI†) revealed a sustained decline, especially in the BFTO3 film with the largest J values. Increased leakage current with decreasing film grain size has also been reported.[31,32]

On the other hand, oxygen vacancies are widely reported as one of the major conducting origins for BFTOs materials. The increase in oxygen vacancies owing to the enhancement of the crystallite size, as well as the decrease in grain boundaries, will lead to the increasing of J_{max}.[33] Meanwhile, as the perovskite-like layers increased, *e.g.* FeO_6 octahedral layers, the amount of oxygen vacancies increased with increasing of such octahedral layers owing to the valence change of iron ions, which resulted in J_{max} increasing. Such defect-relative conductance is remarkable in the high electric field regions.

For metal–ferroelectric–metal configuration, impurity ion conductance, injected electrons (or holes) conductance and extrinsic defects carrier conductance are the main factors influencing the film conductivity at room temperature. The conduction mechanisms can be ascribed to interface-limited conduction, Schottky emission and Fowler–Nordheim tunneling (FN), bulk limited conduction, space-charge-limited current (SCLC) and the Poole–Frenkel (PF) effect. In order to understand the origin of the leakage current, the leakage current mechanism was studied by the various above-mentioned conduction mechanisms. If the leakage is controlled by the PF emission, which originates from the field-assisted thermal ionization of trapped carriers into the conduction band of the semiconductors, then the leakage current density can be expressed as:[34]

$$J_{PF} = cE \exp\left[\frac{e\left(\sqrt{eE/\pi\varepsilon_0\varepsilon_{r0}} - E_t\right)}{kT}\right]$$

where c and e are a constant and electronic charge, k and T are the Boltzmann constant and temperature in Kelvin, ε_0 and ε_{r0} are the permittivity of free space and optical dielectric constant of the film, and E_t is the trap ionization energy. The PF emission produces a linear relation between $\ln J/E$ and $E^{1/2}$. The interface-limited FN tunneling, which may substantially contribute to the leakage current at high applied electric fields, can be described by the following relationship:[35]

$$J_{FN} = BE^2 \exp(C\varphi_i^{3/2}/E)$$

where B and C are the constants and φ_i is the potential barrier height. If the leakage current is dominated by the FN tunneling mechanism, the plot of $\ln J/E^2 - 1/E$ should be a straight line. However, no linear relations were observed both in the PF emission model with $\ln J/E$ *versus* $E^{1/2}$ (see Fig. 2(b)) and the FN tunneling model with $\ln J/E^2$ *versus* $1/E$ (see Fig. 2(c)). Thus, the dominant leakage behaviors of the BFTOs films are neither PF emission nor FN tunneling. The interface-limited Schottky emission (SE), which is based on the Schottky barrier at the interface of the metal electrode and the dielectric, can be described by:[34,36]

$$J_{SE} = AT^2 \exp\left(-\frac{\varphi_b}{kT}\right)\exp\left(\frac{e\sqrt{eE/4\pi\varepsilon_0\varepsilon_{r0}}}{kT}\right)$$

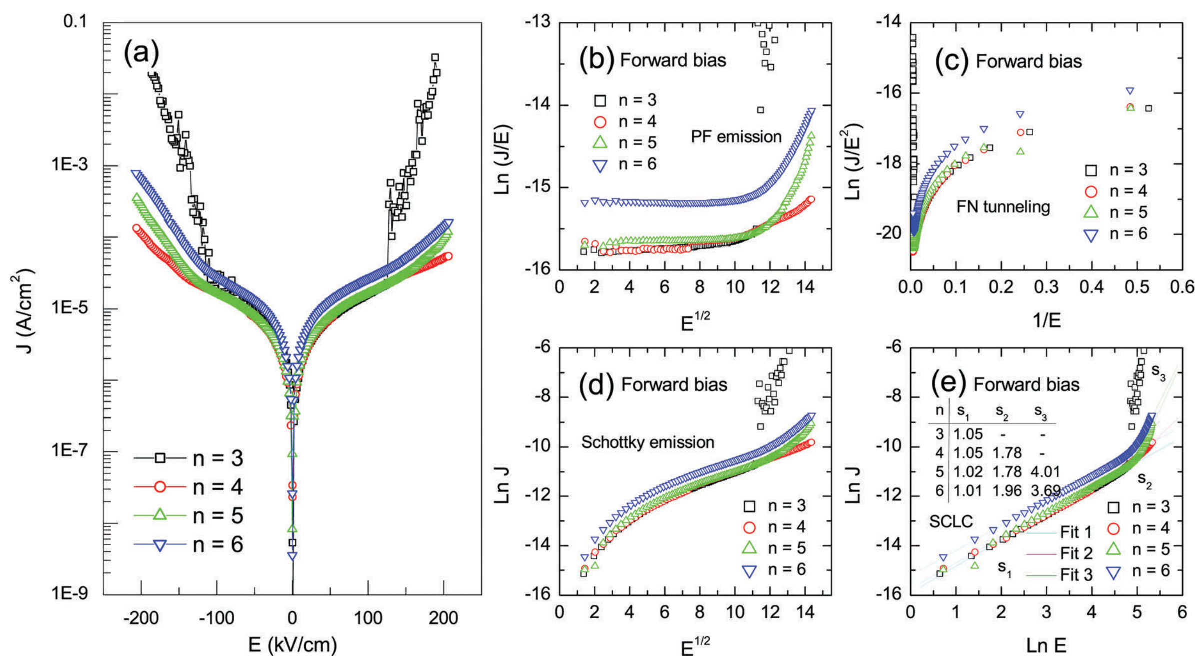

Fig. 2 Leakage current characteristics and relevant current mechanisms of $Bi_4Bi_{n-3}Fe_{n-3}Ti_3O_{3n+3}$ thin films. (a) Leakage current J–E curves in semi-log scales of all derived films. Various fits of the current mechanisms are shown: (b) PF emission $\ln(J/E)$ *versus* $E^{1/2}$ curves, (c) FN tunnelling $\ln(J/E^2)$ *versus* $1/E$ curves, (d) Schottky emission $\ln J$ *versus* $E^{1/2}$ curves, (e) SCLC: space charge limits current $\ln J$ *versus* $\ln E$ curves, where s is the slope. There are no linear relations both in the PF emission model with $\ln J/E$ *versus* $E^{1/2}$ and the FN tunneling model with $\ln J/E^2$ *versus* $1/E$. It was also observed that there is no linear relationship between $\ln J$ and $E^{1/2}$ as the Schottky emission model.

where A is the Richardson constant and φ_b is the Schottky barrier height. If the interface leakage current is indeed controlled by the Schottky emission, a linear relation between $\ln J$ and $E^{1/2}$ should be observed. However, no linear relations were observed in the Schottky emission model with $\ln J$ *versus* $E^{1/2}$, as show in Fig. 2(c). Thus, the interface-limited-conduction mechanism Schottky emission can be excluded.

The anomaly of J values in BFTO3 suggests that the conduction mechanisms has significantly changed or transformed. The changes are confirmed by fitting the J–E curves derived from the results shown in Fig. 2(d). A power law relationship $\ln(J) - s\ln(E)$ is used to fit the curves, where s is the slope. As shown in Fig. 2(d), under weaker electric fields the BFTO3 thin films are known to follow an ohmic conduction mechanism with a slope value of $s \sim 1$, which is represented by the following equation:[37]

$$J_{\text{Ohmic}} = e\mu N_e E$$

where e is the electron charge, μ is the free carrier mobility, N_e is the density of the thermally stimulated electrons, and E is the applied electric field. As shown in Fig. 2(d), under a medium electric field the charge injection from the electrodes into the ferroelectric film leads to the leakage current density exhibiting nonlinear behavior and the value of the slope changes from 1 to 2 for the BFTO4 thin film, indicating a transition of the conduction mechanism from ohmic to SCLC. The leakage current density for the SCLC mechanism is given by:[37]

$$J_{\text{SCLC}} = \left(\frac{9\mu\varepsilon_0\varepsilon_r\theta V^2}{8d^3}\right)$$

where ε_0 and ε_r are the permittivity of free space and static dielectric constant, respectively. Furthermore, V and d are the applied voltage and the thickness of the thin film, respectively. θ denotes the ratio of the total density of free electrons to trapped electrons. The space-charge-limited electric field E_{SCLC} (at which there are the conduction crossovers from ohmic to SCLC type) are shown in Table 1. When the strength of the applied electric field is increased even further, the BFTO5 and BFTO6 thin films exhibit a change in the value of the slope to greater than two ($s \sim 4$), which implies a trap-filled limit (TFL) conduction mechanism.[38] The abrupt increase in leakage current may originate from all the available traps becoming filled by the applied voltage, which can be well explained by the trap-filled-limit law.[37] The electric field at which this abrupt increase occurs is called the trap-filled-limit electric field and is symbolized by E_{TFL}. The E_{TFL} is determined by the law relationship, $E_{\text{TFL}} = eN_t d/2\varepsilon_r\varepsilon_0$, where N_t is unfilled traps density, $N_t = H_a - P_t$, H_a is the total traps density, P_t is the filled traps density, d is the thickness of the film, ε_r is the film's relative permittivity, and e is the electron charge.[31] The E_{TFL} results with n perovskite-like layers are shown in Table 1. In addition,

Table 1 The values of E_{SCLC}, E_{TFL} and N_t

n	E_{SCLC} (kV cm^{-1})	E_{TFL} (kV cm^{-1})	N_t ($\times 10^{17}$ cm^{-3})
3	—	—	—
4	116	—	—
5	107	155	1.03
6	117	156	0.69

 This journal is © The Royal Society of Chemistry 2018

combining the film thickness and measured dielectric constant (see Fig. S3, ESI†), the value of N_t is calculated and it is also presented in Table 1. It is observed that the value of N_t decreased with increasing n, and exhibited a different behavior compared with the E_{SCLC} and E_{TFL}. The decrease in N_t with increased perovskite-like layers n may result from the competition between the total trap density and the concentration of carriers in filled traps. The decrease in oxygen vacancies owing to the reduced crystallite size, which act as one type of charge trapping center, will lead to a reduction of H_a.[33] This will result in a decrease in the value of N_t. On the other hand, the extent of grain boundaries will be increased with the increasing n, and P_t will be decreased due to the decreasing of carrier injection or leakage current density, which will lead to the increase in N_t.

Briefly, the conduction mechanisms of the CSD-derived BFO thin films are described below: under a low electric field, current/voltage follows Ohm's law; under medium electric field, the charge injection from the electrodes into the ferroelectric film follows the conductive mechanism of the space charge limited current model; in high voltage field, the trap-filled-limit law participates in the conduction process. At the same time, the ionic conductivity and electron hopping conductivity also make important contributions to the conductance of the BFTO3 thin film with FN tunneling mechanism in high electric fields.

Ferroelectric properties

Polarization switching is induced by an applied electric field oriented along the film normal between an evaporation surface electrode and a planar bottom electrode, which is a typical configuration of a parallel plate capacitor. The room temperature ferroelectricity of all thin films is measured in the above capacitor-type configuration, and representative results are shown in Fig. 3. To check that the polarization responds to an applied electric field and frequency, we measured the ferroelectric polarization–electric field (P–E) hysteresis loops in the different applied electric fields and frequencies, as shown in Fig. 3(a) and (b), which use BFTO4 as an example (for other films see ESI,† in Fig. S4 and S5).

Firstly, with increasing applied electric field, the BFTO4 thin film exhibits well-shaped rectangular ferroelectric hysteresis loops in the maximum applied electric field up to 800 kV cm^{-1} and the squareness of the loops was well improved. A high electric field on the as-grown BFTO4 film without breakdown indicates the high quality of the film for its dense and smooth surface morphology (as shown in Fig. S2, ESI†). The remanent polarization ($2P_r$ defined as the double polarization at the zero electric field) value of the present film can reach as high as 46 μC cm^{-2}, which is comparable to the sol–gel grown un-doped and La-, Nd- and Co-doped $BTFO_4$ thin films reported by other groups with excellent rectangularity,[39–42] whereas this value is larger than the values of PLD-grown BTFO films due to the preferential orientation of the latter.[43,44] Similar scenarios also appeared in the BFTO5 films, and there are very few reports on BFTO6 films at present.[45–48] The P_{max} (polarization at larger electric field) of 40 μC cm^{-2} almost reached the theoretical value.[28] These values are comparable to those in the rare-earth-substituted BFTO3 thin films, which have been widely studied as candidates for lead-free ferroelectrics and components of non-volatile FeRAM.[24] It is noted that a well-defined P–E hysteresis loop

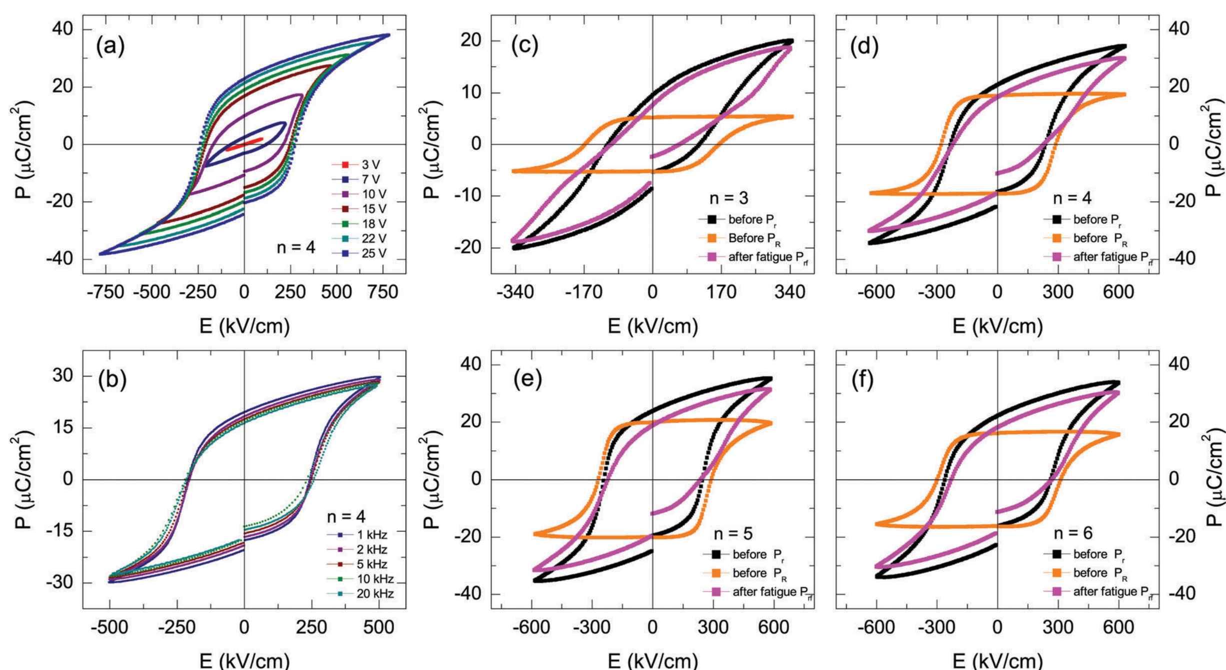

Fig. 3 Ferroelectric polarization–electric field (P–E) hysteresis loops of all derived thin films at room temperature. (a) P–E loops in the different applied electric field and (b) frequency of BFTO4 thin film as a representative example. P–E hysteresis loops of (c) BFTO3, (d) BFTO4, (e) BFTO5 and (f) BFTO6 in similar applied field and frequency (besides BFTO3, for details see main text). Three species of hysteresis loops are plotted. They are the initial polarization curve (black line), fatigued polarization curve (magenta line) and remanent polarization curve (orange line).

This journal is © The Royal Society of Chemistry 2018

can be obtained when the applied electric field is beyond 400 kV cm^{-1}, as shown in Fig. 2(a). Similar results for the BFTO5 and BFTO6 films are shown in Fig. S4 (ESI†). However, no remanent polarization or high leaky characteristics were observed for BFTO5 and BFTO6 films in the previous results.[17,44,48,49]

Secondly, with increasing applied frequency, the BFTO4 thin film exhibits a well-shaped ferroelectric hysteresis loop in the maximum applied frequency up to 20 kHz and the squareness of the loops was well retained. Careful observation reveals that the values of $2P_r$ showed a continuous decline but coercive electric field ($2E_c$ defined as the double electric field at the zero polarization) demonstrates an inverse tendency (see ESI,† Fig. S6). Note that in practical measurement, hysteresis circuits do not measure polarization directly. Rather, they measure the switched charge, as mentioned above. For an ideal ferroelectric insulator $Q = 2P_rA$, where P_r is the remanent polarization and A is the electrode area for a parallel-plate capacitor. For a somewhat conductive sample $Q = 2P_rA + \sigma E_a t$, where σ is the electrical conductivity, E_a is the applied field, and t is the measuring time.[50] Thus Q in a pulsed measuring system depends on the pulse width. It will be a serious problem if conductivity is large. From the above equation, the Q decreased as frequency increased owing to the films' conductivity, leading to the continuous decline of $2P_r$ values. The squareness of the loops is well retained (see Fig. S5 in ESI†) and the degree of the P_r decrease is 14.8%, 15%, 24.7% and 25.3% for BFTO3, BFTO4, BFTO5 and BFTO6 when applying a frequency from 1 kHz to 20 kHz, respectively. The observed variation in the apparent polarization of BFTO4 is shown in the ESI,† in Fig. S6(a). The significant increase in the apparent polarization at low frequencies indicates the presence of mobile free charges, which may be responsible for the leaky nature of the films.

These free charge carriers can be of defect dipole complexes $Fe'_{Fe^{3+}}V_O^{\bullet\bullet}$ and oxygen vacancies $V_O^{\bullet\bullet}$, which could be produced in these materials owing to the valence fluctuation of Fe ions during the heat treatment of the films. However, at high frequencies, the apparent polarization is found to be nearly constant, which indicates that the polarization in this region is mainly originated from the ferroelectric switching. On the other hand, polarization switching in ferroelectrics has been thought to occur through the nucleation and growth of new domains follows the Ishibashi–Orihara model, although the nucleation process can be suppressed in sufficiently thin films.[51] In this model one considers a nucleus formed at a time and then a domain propagating outwards from it with velocity. The result of the model is that the fraction of switched charge Q as a function of field and frequency may be expressed as $Q(E, f) = 1 - \exp[-f^{-D}\Phi(E)]$, where D is the dimensionality of the growth and $\Phi(E)$ depends on the wave form used for switching.[52] It can be deduced that switched charge will decrease as the frequency increases in the same applied electric field. Actually, the present feature of frequency-dependent polarization has been observed in ferroelectric thin films, ceramics and single crystals, so it seems impossible to avoid it.[50] In turn, it provides the methodology to research the dynamics of polarization switching. It is reasonable to say that frequency response is not only interesting in fundamental physics research but also has a guiding significance for practical applications. Because of the slight offsets in the measured P–E hysteresis loops, the experimental E_c values were determined by using $E_c = (E_c^+ + E_c^-)/2$, where E_c^+ and E_c^- are the magnitudes of the positive and negative electric field values at zero polarization, respectively. The small applied-field offsets were possibly due to built-in fields in the ferroelectric films or different work functions of the electrode. Based on the Ishibashi–Orihara model, after some consideration and the substitution of $\Phi(E) = E^k$ in the above equation, a useful relationship for the dependence of the field on frequency can be obtained as $E_c = f^{D/k}$. It can be seen that E_c increases as f increases (see Fig. S6(b) in the ESI†).

To explore the layer effect on the ferroelectric, P–E hysteresis loops of all derived films are shown on the right side of Fig. 3 in the same applied field and frequency (lower field for BFTO3 due to breakdown). There are three species of hysteresis loops plotted in Fig. 3: initial polarization curve (black line), fatigued polarization curve (magenta line) and remanent polarization curve (orange line). We will use those three loops to discuss the ferroelectric of different n.

First of all, we focus on the initial and remanent polarization loops, and the correlation between them. It is observed that all films showed well-shaped ferroelectric hysteresis loops in the applied field. The BFTO3 film's P–E loop is comparable to the results obtained by CSD and PLD, while the others almost reached the best value of those materials in the present literature. Variation of P_r and E_c with n is shown in Fig. 4(f). It is can be seen that P_r showed a sharp increase with n increasing from 3 to 4, and kept on increasing up to n = 5 then reached a plateau region at n = 6. This variation tendency is also seen in the n dependence E_c, as shown in Fig. 4(f). Several factors could be considered to understand this change of ferroelectric behavior. First, Aurivillius compounds have a strong anisotropy in the spontaneous polarization along with the layered crystallographic features.[24] That is, c axis-oriented

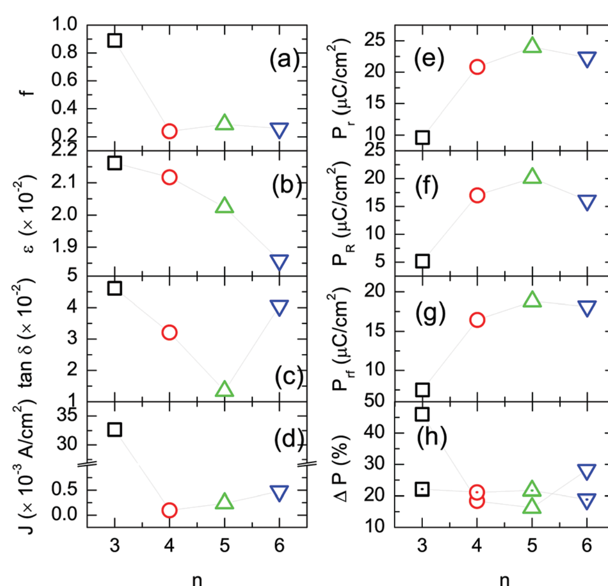

Fig. 4 Ferroelectric thin films' related parameters evolution with n perovskite-like layers. For details, please refer to the corresponding text section.

films have a negligible polarization component along the film normal, because the vector of the major spontaneous polarization in these layered perovskite materials is along the *a* axis. The orientation of all films evaluated by Lotgering factor *f* is shown in Fig. 4(d). The smallest P_r of the BFTO3 sample could mainly be attributed to the largest *f* value compared to other samples. In addition, the leakage density of BFTO3 (shown in Fig. 2(a)) is larger than that of the rest of samples, as discussed in the preceding part of the text. This is another reason for the smaller P_r in BFTO3, owing to the fact that the thin film is inclined to breakdown with larger leakage density. Compared to the other three films the lower breakdown electric field of BFTO3 is noticeable in Fig. S4 (ESI†). Second, types of atomic motions involved in the lowering symmetry leading to the ferroelectric ground state can depend on the chemical composition. Usually they include (i) tilts of the oxygen octahedra around the *a*-axis, (ii) rotations of the oxygen octahedra around the *c*-axis and (iii) polar cation motions along the *a*-axis, *i.e.*, the (110) direction of the tetragonal reference structure.[12] Introducing the Fe ion (or Fe–O octahedral) to the B-site of Aurivillius compounds, *i.e.*, perovskite-like layer, gives rise to the distortion of the crystal structure owing to the ionic radius difference between Fe^{3+} (0.645 Å) and Ti^{4+} (0.605 Å). This distorted structure holds a larger polarization as evidenced through first principles calculation by Birenbaum and his co-worker.[53] In some cases, a layer-insertion concept is used to describe such layered Aurivillius materials with higher *n*. For example, *via* insertion of quantitative $BiFeO_3$ into $Bi_4Ti_3O_{12}$, $Bi_5FeTi_3O_{15}$, $Bi_6Fe_2Ti_3O_{18}$ and $Bi_7Fe_3Ti_3O_{21}$ are obtained just as reported here. Even average period of $n = 9$ $Bi_{10}Fe_6Ti_3O_{30}$ ceramics and $n = 10$ $Bi_{11}(Fe_5CoTi_3)_{10/9}O_{33}$ epitaxial thin films have been obtained recently.[8,54] Following this concept, two prototypical ferroelectric materials are hybrids at the molecular level, one is the material that has the largest remanent polarization and the other is the material that has good fatigue endurance properties by some lanthanide doping. Those two parameters are very important for applications in ferroelectric random access memory (FeRAM).

Then, in order to eliminate the extrinsic contributions, such as leakage current and interface to *P–E* loop in the thin films, we performed Positive-Up Negative-Down (PUND) measurements, which extract only the hysteresis component (intrinsic contribution) automatically without any assumptions.[55] The ferroelectric hysteresis of all thin films is measured by such PUND method and the results are shown in Fig. 3. Rectangular *P–E* loops (orange line) with no obvious polarization gap are obtained by PUND, compared to the loops (black line) obtained by the conventional polarization measurements with the same applied field and frequencies. It was reasonable that the $2P_r$ values obtained from the PUND measurements discussed above were smaller than the conventional *P–E* measurements owing to the elimination of the extrinsic contributions. Especially for BFTO3, which showed a larger leakage current, the values of remanent polarization showed a decrease of 45% from 9.6 $\mu C\ cm^{-2}$ to 5.2 $\mu C\ cm^{-2}$. The difference between the $2P_r$ (from conventional *P–E*) and $2P_r$ (from PUND *P–E*) values for BFTO4, BFTO5 and BFTO6 is 18%, 17%, and 28%, respectively, shown in Fig. 4(h) as hollow symbol representation. This implies that the contribution of the leakage current to the remanent polarization is insignificant, especially for BFTO4 and BFTO5, which showed the smallest leakage current. The PUND measurement results confirm that the obtained larger remanent polarization is from the intrinsic ferroelectric domain switching contribution.

In addition, the ferroelectric fatigue and retention properties, which play a key role in determining the performance and lifetime of ferroelectric-based devices, as discussed above, have also been tested.[50] The corresponding polarization dependent on the relaxation times and the read/write switching cycles results are shown in Fig. S7 and S8 (ESI†). Apart from BFTO3, the polarizations approached a near steady-state value after a retention time of 2×10^4 s, which implied that the retained switchable polarization is stable. The fatigued polarization loops of all derived thin films are shown in Fig. 3 (magenta line). The values of P_r before the fatigue test are 9.6, 20.8, 24 and 22.4 $\mu C\ cm^{-2}$ for the respective layer number *n*, as shown in Fig. 4(e). After the sample is subjected to 1×10^{10} cycles, the P_{rf} (indicating P_r after fatigue test as shown in Fig. 4(g)) values remain at 7.5, 16.5, 18.8 and 18.1 $\mu C\ cm^{-2}$, respectively. The switchable polarization loss after read/write switching cycles is 21.8%, 20.7%, 21.6%, and 19.2%, shown in the Fig. 4(h) as hollow with point symbol representation. All films showed similar values of switchable polarization loss. However, in contrast to the BFTO3 with smaller P_r and deformed *P–E* loop, the remaining three kinds of films not only have definitely larger P_r, but also conformal *P–E* loops. Such larger switchable polarization with well-defined *P–E* loops and stable retention properties suggested that BFTO films with higher *n* are potential candidates for memory applications.

Conclusions

Ferroelectric thin films $Bi_4Bi_{n-3}Fe_{n-3}Ti_3O_{3n+3}$ (BFTO $n \geq 3$) were successfully grown on platinum-coated silicon substrate by chemical solution deposition. The crystallography, XRD and HR-TEM microstructure analysis results confirmed the layer structure evolution from $n = 3$ to 6 with Aurivillius phase. Owing to the combination of oxygen vacancies and grain size effect, the leakage current gradually increased with the increasing of *n*. The conduction mechanisms of the CSD-derived BFO thin films are electric-field dependent: Ohm's law, the conductive mechanism of space charge limited current model and the trap-filled-limit law play a dominant role under a low electric field, medium electric field and high voltage field, respectively. Moreover, the BFTO3 thin film showed FN tunneling mechanism in high electric field with ionic conductivity and electron hopping conductivity. The saturated hysteresis loop with larger remanent polarization ($2P_r$) and excellent retention properties are observed in all thin films. The values of $2P_r$ in the $n = 4$, 5 and 6 thin films are all about 50 $\mu C\ cm^{-2}$ with rectangular ferroelectric hysteresis loops and covering a wide range of frequencies. Larger remanent polarization combined with favorable fatigue and retention performances are very important in ferroelectric data storage devices and these are also promising to further explore single-phase multiferroics in Aurivillius thin films.

This journal is © The Royal Society of Chemistry 2018

Conflicts of interest

There are no conflicts to declare.

Acknowledgements

This work was supported by the Joint Funds of the National NSFC (Grant No. U1432137), the Natural Science Foundation of the Higher Education Institutions of Jiangsu Province (17KJB140006), and the Scientific Research Foundation of Jiangsu University of Science and Technology (No. 1052931611).

Notes and references

1 G. A. Smolenskii, V. A. Isupov and A. I. Agranovskaya, *Phys. Solid State*, 1959, **1**, 149–150.
2 E. C. Subbarao, *J. Phys. Chem. Solids*, 1962, **23**, 665–676.
3 J. F. Scott, *NPG Asia Mater.*, 2013, **5**, e72.
4 R. K. Vasudevan, Y. Matsumoto, X. Cheng, A. Imai, S. Maruyama, H. L. Xin, M. B. Okatan, S. Jesse, S. V. Kalinin and V. Nagarajan, *Nat. Commun.*, 2014, **5**, 4971.
5 S. Kooriyattil, R. K. Katiyar, S. P. Pavunny, G. Morell and R. S. Katiyar, *Appl. Phys. Lett.*, 2014, **105**, 072908.
6 G. Naresh and T. K. Mandal, *ACS Appl. Mater. Interfaces*, 2014, **6**, 21000–21010.
7 J. Wang, Z. Fu, R. Peng, M. Liu, S. Sun, H. Huang, L. Li, R. J. Knize and Y. Lu, *Mater. Horiz.*, 2015, **2**, 232–236.
8 Y. Huang, G. Wang, S. Sun, J. Wang, R. Peng, Y. Lin, X. Zhai, Z. Fu and Y. Lu, *Sci. Rep.*, 2015, **5**, 15261.
9 Y. Zhao, H. Fan, X. Ren, C. Long, G. Liu and Z. Liu, *J. Mater. Chem. C*, 2016, **4**, 7324–7331.
10 X. Z. Z. Cui, Y.-D. Chuang, H. Xu, H. Huang, J. Wang, Z. Fu, R. Peng, J. Guo and Y. Lu, *Phys. Rev. B*, 2017, **95**, 205102.
11 A. Y. Birenbaum, A. Scaramucci and C. Ederer, *Phys. Rev. B*, 2017, **95**, 104419.
12 N. A. Benedek, J. M. Rondinelli, H. Djani, P. Ghosez and P. Lightfoot, *Dalton Trans.*, 2015, **44**, 10543–10558.
13 J. Yang, W. Tong, Z. Liu, X. B. Zhu, J. M. Dai, W. H. Song, Z. R. Yang and Y. P. Sun, *Phys. Rev. B: Condens. Matter Mater. Phys.*, 2012, **86**, 104410.
14 Z. Lei, M. Liu, W. Ge, Z. Li, R. J. Knize and Y. Lu, *Mater. Lett.*, 2015, **139**, 348–351.
15 G. Wang, Y. Huang, S. Sun, J. Wang, R. Peng and Y. Lu, *J. Am. Ceram. Soc.*, 2016, **99**, 1318–1323.
16 H. Zhao, K. Cai, Z. Cheng, T. Jia, H. Kimura, Z. Ma, Q. Fu, Z. Huang, T. Matsumoto, T. Tohei, N. Shibata and Y. Ikuhara, *Adv. Electron. Mater.*, 2017, **3**, 1600254.
17 J. Wang, H. Huang, C. Liu, Z. Fu, X. Zhai, R. Peng and Y. Lu, *Appl. Phys. Lett.*, 2015, **106**, 132903.
18 N. A. Lomanova, I. V. Pleshakov, M. P. Volkov and V. V. Gusarov, *Mater. Sci. Eng., B*, 2016, **214**, 51–56.
19 J. B. Li, Y. P. Huang, G. H. Rao, G. Y. Liu, J. Luo, J. R. Chen and J. K. Liang, *Appl. Phys. Lett.*, 2010, **96**, 222903.
20 J. F. Scott, *J. Phys.: Condens. Matter*, 2008, **20**, 021001.
21 D. P. Song, J. Yang, Y. X. Wang, L. Y. Chen, Y. Q. Chu and X. B. Zhu, *Phys. Status Solidi RRL*, 2017, **11**, 1700278.
22 B. Yang, D. Song, L. Jin, X. Tang, J. Yang, J. Dai, W. Song, X. Zhu and Y. Sun, *J. Alloys Compd.*, 2017, **694**, 489–496.
23 N. Zhong, P.-H. Xiang, Y.-Y. Zhang, X. Wu, X.-D. Tang, P.-X. Yang, C.-G. Duan and J.-H. Chu, *J. Appl. Phys.*, 2015, **118**, 104102.
24 H. N. Lee, D. Hesse, N. Zakharov and U. Gosele, *Science*, 2002, **296**, 2006–2009.
25 X. Li, Z. Zhu, F. Li, R. Peng, X. Zhai, Z. Fu and Y. Lu, *J. Eur. Ceram. Soc.*, 2015, **35**, 3437–3443.
26 J. P. a. D. V. B. Meyer, *Faraday Discuss.*, 1999, **114**, 395–405.
27 W. S. Choi, M. F. Chisholm, D. J. Singh, T. Choi, G. E. Jellison, Jr. and H. N. Lee, *Nat. Commun.*, 2012, **3**, 689.
28 A. Y. Birenbaum and C. Ederer, *Appl. Phys. Lett.*, 2016, **108**, 082903.
29 N. A. Lomanova, V. G. Semenov, V. V. Panchuk and V. V. Gusarov, *J. Alloys Compd.*, 2012, **528**, 103–108.
30 L. Keeney, C. Downing, M. Schmidt, M. E. Pemble, V. Nicolosi and R. W. Whatmore, *Sci. Rep.*, 2017, **7**, 1737.
31 X. W. Tang, J. M. Dai, X. B. Zhu, J. C. Lin, Q. Chang, D. J. Wu, W. H. Song and Y. P. Sun, *J. Am. Ceram. Soc.*, 2012, **95**, 538–544.
32 T. Jia, H. Kimura, Z. Cheng and H. Zhao, *J. Alloys Compd.*, 2015, **632**, 473–477.
33 G. D. V. A. R. Venkateswarlu and R. Nath, *AIP Adv.*, 2011, **1**, 042140.
34 F. Yang, F. Zhang, G. Hu, Z. Zong and M. Tang, *Appl. Phys. Lett.*, 2015, **106**, 172903.
35 H. Yang, M. Jain, N. A. Suvorova, H. Zhou, H. M. Luo, D. M. Feldmann, P. C. Dowden, R. F. DePaula, S. R. Foltyn and Q. X. Jia, *Appl. Phys. Lett.*, 2007, **91**, 072911.
36 G. W. Pabst, L. W. Martin, Y.-H. Chu and R. Ramesh, *Appl. Phys. Lett.*, 2007, **90**, 072902.
37 C. Wang, M. Takahashi, H. Fujino, X. Zhao, E. Kume, T. Horiuchi and S. Sakai, *J. Appl. Phys.*, 2006, **99**, 054104.
38 D. P. Song, J. Yang, B. Yuan, X. Z. Zuo, X. W. Tang, L. Chen, W. H. Song, X. B. Zhu and Y. P. Sun, *J. Appl. Phys.*, 2015, **117**, 244105.
39 Y. Li, C. J. Lu, J. Su, Y. C. Zhang, C. Zhang, S. F. Zhao, X. X. Wang, D. J. Zhang and H. M. Yin, *J. Alloys Compd.*, 2016, **687**, 707–711.
40 W. Bai, J. Y. Zhu, J. L. Wang, T. Lin, J. Yang, X. J. Meng, X. D. Tang, Z. Q. Zhu and J. H. Chu, *J. Magn. Magn. Mater.*, 2012, **324**, 2265–2270.
41 H. Sun, X. Lu, J. Su, T. Xu, C. Ju, F. Huang and J. Zhu, *J. Phys. D: Appl. Phys.*, 2012, **45**, 385001.
42 C. Zhang, J. Su, C. Lu, Y. Zhang, Y. Li, L. Feng, D. Zhang, H. Yin and Y. Huang, *J. Mater. Sci.*, 2017, **52**, 6138–6145.
43 S. Kooriyattil, S. P. Pavunny, D. Barrionuevo and R. S. Katiyar, *J. Appl. Phys.*, 2014, **116**, 144101.
44 H. Zhao, H. Kimura, Z. Cheng, M. Osada, J. Wang, X. Wang, S. Dou, Y. Liu, J. Yu, T. Matsumoto, T. Tohei, N. Shibata and Y. Ikuhara, *Sci. Rep.*, 2014, **4**, 5255.
45 W. Bai, W. F. Xu, J. Wu, J. Y. Zhu, G. Chen, J. Yang, T. Lin, X. J. Meng, X. D. Tang and J. H. Chu, *Thin Solid Films*, 2012, **525**, 195–199.
46 H. Sun, B. Zou, X. Ni, X. Mao, X. Chen and J. Zhu, *J. Mater. Sci.*, 2015, **50**, 5475–5481.
47 Y. Yun, X. Zhai, C. Ma, H. Huang, D. Meng, Z. Cui, J. Wang, Z. Fu, R. Peng, G. J. Brown and Y. Lu, *Appl. Phys. Express*, 2015, **8**, 054001.

 This journal is © The Royal Society of Chemistry 2018

48 S. J. Patwe, S. N. Achary, J. Manjanna, A. K. Tyagi, S. K. Deshpande, S. K. Mishra, P. S. R. Krishna and A. B. Shinde, *Appl. Phys. Lett.*, 2013, **103**, 122901.

49 X. N. Li, Z. Ju, F. Li, Y. Huang, Y. M. Xie, Z. P. Fu, R. J. Knize and Y. L. Lu, *J. Mater. Chem. A*, 2014, **2**, 13366–13372.

50 L. Jin, F. Li, S. Zhang and D. J. Green, *J. Am. Ceram. Soc.*, 2014, **97**, 1–27.

51 H. Orihara, S. Hashimoto and Y. Ishibashi, *J. Phys. Soc. Jpn.*, 1994, **63**, 1031–1035.

52 M. Dawber, K. M. Rabe and J. F. Scott, *Rev. Mod. Phys.*, 2005, **77**, 1083–1130.

53 A. Y. Birenbaum and C. Ederer, *Phys. Rev. B: Condens. Matter Mater. Phys.*, 2014, **90**, 214109.

54 D. Meng, X. Zhai, C. Ma, H. Huang, Y. Yun, Y. Huang, Z. Fu, R. Peng, X. Mao, X. Chen, G. Brown and Y. Lu, *Appl. Phys. Lett.*, 2015, **106**, 212906.

55 Y. S. Chai, Y. S. Oh, L. J. Wang, N. Manivannan, S. M. Feng, Y. S. Yang, L. Q. Yan, C. Q. Jin and K. H. Kim, *Phys. Rev. B: Condens. Matter Mater. Phys.*, 2012, **85**, 184406.